https://doi.org/10.5194/ms-2026-209
Preprint. Discussion started: 27 November 2026
© Author(s) 2026. CC BY 4.0 License.



mechanical sciences
DISCUSSIONS

Local linear control of high-frequency rotary ultrasonic micromachining systems based on a load-prediction model

Kuan Zhang[1], Guochang Zhu[1], Yanqiu Xiao[1,2], Guangzhen Cui[1,2], Jiakang Guo[1], Xiaoyu An[1]

[1]Henan School of Excellent Engineers, Zhengzhou University of Light Industry, Zhengzhou 450000, China
[2]Collaborative Innovation Center of Intelligent Tunnel Boring Machine, Henan Province, China

Correspondence to: Kuan Zhang (zhangkuan@zzuli.edu.cn)

Abstract. The efficacy of dynamic resonant frequency tracking and constant amplitude regulation is intrinsically linked to the machining precision and throughput of rotary ultrasonic micromachining (RUM). However, conventional feedback control architectures are significantly constrained by the high-speed rotational characteristics of the ultrasonic spindle, which impedes direct sensor-based load-side feedback. To enhance the control performance under axial loads ranging from 0 to 10 N, this study first investigates the response characteristics of impedance magnitude and phase in a high-frequency ultrasonic system equipped with a bilateral matching network. Subsequently, functional response relationships between the resonant frequency, impedance, and phase are established under varying load conditions. An ensemble radial basis function–extreme learning machine framework is then developed for real-time cutting force estimation, enabling the dynamic update of reference setpoints for resonant frequency and excitation current. Furthermore, fuzzy domains and control rules for the fuzzy proportional–integral–derivative (PID) algorithm are formulated to maintain operational stability. The methodology proposed in this study provides a robust theoretical foundation for achieving high-precision and high-efficiency rotary ultrasonic micromachining.

Keywords. Piezoelectric transducer; Load characteristics; Ultrasonic micromachining; Local linear control

1 Introduction

Rotary ultrasonic micromachining (RUM) has emerged as a cornerstone of advanced precision manufacturing, leveraging its superior efficiency, high accuracy, and minimized subsurface damage when processing difficult-to-machine materials characterized by high hardness and toughness (Ansary et al., 2025; Zhang et al., 2005; Xu et al., 2017). However, machining efficacy and surface integrity are fundamentally contingent upon the system's robustness in maintaining dynamic resonant frequency tracking and constant amplitude output under complex transient loading conditions (Zhang et al., 2024a; Tang et al., 2023). Particularly in high-speed rotary ultrasonic spindles, the acquisition of real-time load-side feedback signals and implementation of closed-loop control face significant challenges due to the inherent rotational characteristics, thus restricting further improvements in system performance (Quan et al., 2023; Du et al., 2023). Control strategies for ultrasonic vibration systems have evolved from conventional single-parameter tracking toward integrated multivariable control (Du et

https://doi.org/10.5194/ms-2026-209
Preprint. Discussion started: 27 November 2026
© Author(s) 2026. CC BY 4.0 License.



mechanical sciences
DISCUSSIONS

al., 2021; Zhang et al., 2023; Lin et al., 2024). Early investigations primarily focused on accurate resonant frequency tracking using conventional methodologies (Wang et al., 2020; Liu et al., 2015; Ma et al., 2024).

Conventional frequency tracking methodologies, such as maximum current, maximum output power, and admittance circle search, rely on extremum searches of electrical parameters. Although simple to implement, these methods suffer from slow dynamic response, limited robustness against load disturbances, and sensitivity to parameter drift (Wang et al., 2020; Liu et al., 2015; Ma et al., 2024). Phase-locked loop strategies provide high tracking precision and rapid dynamic response but are sensitive to variations in transducer bandwidth and quality factor (Q), potentially causing instability under significant load fluctuations (Lin et al., 2007). Impedance-matching strategies based on static or dynamic LC and LCC topologies can improve energy transmission efficiency and broaden the stable operating range (Jiang et al., 2025). However, static matching remains sensitive to frequency drift, while dynamic matching is often constrained by circuit complexity (Duan et al., 2025; Zhang et al., 2024b). Intelligent control schemes combining fuzzy PID and neural networks, such as RBF and ELM, provide improved adaptability to nonlinear and time-varying loads, enabling coordinated regulation of resonant frequency and vibration amplitude (Du et al., 2021; Lin et al., 2024; Peng et al., 2025). However, their real-time implementation may still be limited by computational complexity and the need for appropriate models or training data. As machining conditions become more complex, resonant frequency tracking alone is insufficient to ensure surface integrity. Load fluctuations induce nonlinear changes in the transducer's motional parameters, including motional inductance L_1, capacitance C_1, and resistance R_1, causing both resonant frequency shifts and significant output amplitude attenuation (Zhu et al., 2026). Consequently, constant amplitude regulation is as important as frequency tracking and requires modulation of the excitation voltage or current to compensate for energy dissipation caused by load impedance variations (Du et al., 2021; Wang et al., 2025; Peng et al., 2025).

Direct installation of feedback sensors on high-speed rotating tool holders is difficult (Du et al., 2023). Current research mainly follows two approaches: indirect load estimation through mappings between mechanical loads and measurable electrical parameters, and real-time load evaluation using artificial intelligence methods (Lin et al., 2024; Mostaghimi et al., 2023). In this study, the relationships between cutting force and system impedance and phase are exploited for load characterization. An ensemble Radial Basis Function-Extreme Learning Machine (RBF-ELM) framework is developed for real-time cutting-force estimation, enabling dynamic updates of the reference resonant frequency and excitation current. This approach provides a data-driven solution to load-side feedback and closed-loop control in high-speed rotary environments.

2 Locally linear load characteristics

Load fluctuations induce variations in the electromechanical parameters of high-frequency rotary ultrasonic systems, which influence resonant frequency stability and vibration amplitude regulation. To characterize these load-dependent behaviors, the impedance response and excitation characteristics of the ultrasonic transducer under varying loads are analyzed.

https://doi.org/10.5194/ms-2026-209
Preprint. Discussion started: 27 November 2026
© Author(s) 2026. CC BY 4.0 License.



mechanical sciences
DISCUSSIONS

2.1 Load impedance matching characteristics

Generally, once the loosely coupled contactless power transfer rotary transformer is fixed, parameters such as coil self-inductance and mutual inductance remain stable, with negligible effects from frequency drift and voltage fluctuations. However, under load fluctuations, the bilateral static matching compensation scheme fails to maintain complete impedance matching for the ultrasonic spindle, causing fluctuations in the equivalent impedance. Furthermore, fixed-parameter PID control struggles to compensate for the steady-state error caused by variations in the reflected impedance. As shown in Fig. 1, the equivalent circuit of an impedance-matched ultrasonic scalpel handle includes a loosely coupled rotary transformer (RT), a piezoelectric ultrasonic transducer represented by the Butterworth-Van Dyke (BVD) model, and an LCC-Series Compensation Topology (LCC-CS) bilateral impedance matching compensation network. The LCC-CS network employs a dynamic LCC on the stationary side of the primary winding and a static CS on the rotating side, forming a dynamic-static bilateral matching network. During circuit analysis, the impedance of the secondary rotating side is reflected onto the primary-side LCC dynamic matching network. As illustrated in Fig. 1, the LCC network on the primary side comprises an inductor L_{m1}, a fixed-value capacitor C_{m11}, and an adjustable capacitor C_{m12}, while the CS network on the secondary side contains a fixed-value capacitor C_{m2}. The equivalent circuit of the rotary transformer (RT) consists of the primary self-inductance L_{t1} and resistance R_{t1}, the mutual inductance M, and the secondary self-inductance L_{t2} and resistance R_{t2}. Furthermore, the BVD equivalent circuit of the piezoelectric ultrasonic transducer includes the clamped capacitance C_0, motional resistance R_{eq}, motional capacitance C_1, and motional inductance L_1.

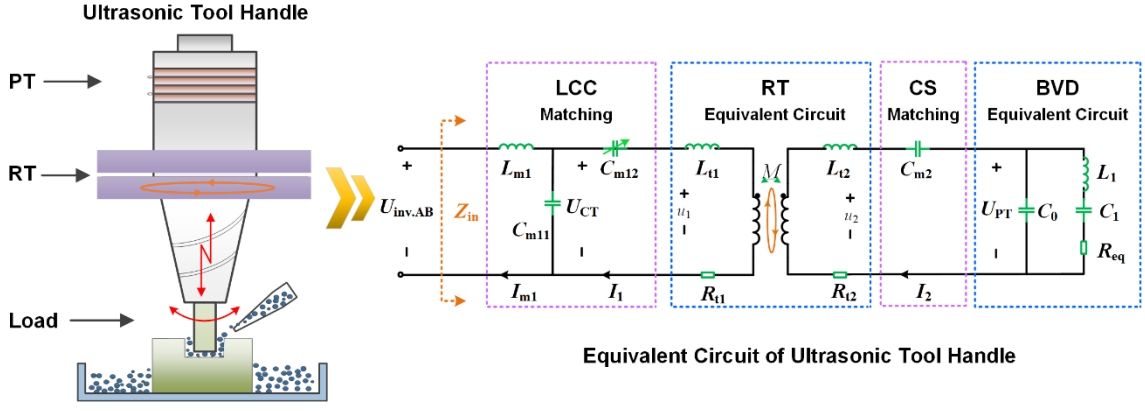

Figure 1: Equivalent circuit of an ultrasonic scalpel handle incorporating an LCC-CS bilateral impedance-matching compensation network.

Under a varying cutting force load, the equivalent impedance and phase at the transducer input are

$$\begin{cases} Z_{PT}(F) = \dfrac{1-\omega_{(F)}^2 L_{1(F)}C_{1(F)}+j\omega_{(F)}C_{1(F)}R_{1(F)}}{j\omega_{(F)}(C_{0(F)}+C_{1(F)}-\omega_{(F)}^2 L_{1(F)}C_{1(F)}C_{0(F)})-\omega_{(F)}^2 C_{1(F)}C_{0(F)}R_{1(F)}} = R_{PT}(F)+jX_{PT}(F) \\ \theta_{PT}(F) = \arctan(X_{PT}(F)/R_{PT}(F)) \end{cases} \quad (1)$$

Z_{PT} represents the input impedance of the piezoelectric ultrasonic transducer, and θ_{PT} is the phase of Z_{PT}.

https://doi.org/10.5194/ms-2026-209
Preprint. Discussion started: 27 November 2026
© Author(s) 2026. CC BY 4.0 License.



mechanical sciences DISCUSSIONS

The equivalent impedance and phase of the rotating side of the ultrasonic handpiece are

$$\begin{cases} Z_2(F) = R_{t2} + j\omega_{(F)}L_{t2} + 1/j\omega_{(F)}C_{m2} + Z_{PT}(F) = R_2(F) + jX_2(F) \\ \theta_2(F) = \arctan(X_2(F)/R_2(F)) \end{cases} \tag{2}$$

Z_2 represents the impedance of the rotating side of the ultrasonic tool holder when there is a static capacitance C_{m2} matching, and θ_2 is the phase of Z_2.

The reflection impedance Z_r, reflected from the rotating side of the secondary side to the stationary side of the primary side is

$$Z_r(F) = \frac{\omega_{(F)}^2 M^2}{Z_2(F)} = R_r(F) + jX_r(F) \tag{3}$$

The equivalent impedance and phase of the input terminal of a rotating transformer are

$$\begin{cases} Z_{RT}(F) = R_{t1} + j\omega_{(F)}L_{t1} + Z_r(F) = R_{RT}(F) + jX_{RT}(F) \\ \theta_{RT}(F) = \arctan(X_{RT}(F)/R_{RT}(F)) \end{cases} \tag{4}$$

The equivalent impedance and phase of the LCC matching network input under variable cutting force load can be obtained as

$$\begin{cases} Z_{in}(F) = j\omega_{(F)}L_{m1} + \frac{1+Z_{RT}(F)\times j\omega_{(F)}C_{m12}}{j\omega_{(F)}(C_{m11}+C_{m12})-Z_{RT}(F)\times\omega_{(F)}^2 C_{m11}C_{m12}} = R_{in}(F) + jX_{in}(F) \\ \theta_{in}(F) = \arctan(X_{in}(F)/R_{in}(F)) \end{cases} \tag{5}$$

The phase response in Fig. 2(a) reveals that the inductive nature of Z_2 decreases as the cutting force increases, while the capacitive nature increases correspondingly. Consequently, static matching alone cannot maintain the piezoelectric ultrasonic transducer in a purely resistive state; nevertheless, the implementation of static matching using capacitor C_{m2} attenuates the capacitive state by approximately 50%. Z_{in_0} denotes the equivalent input impedance of the LCC matching network under the LCC-CS bilateral static matching scheme, where θ_{in_0} represents the phase angle of Z_{in_0}. Similarly, Z_{in_1} represents the equivalent input impedance of the LCC matching network under the LCC-CS bilateral static matching scheme, with θ_{in_1} denoting the corresponding phase angle. Figure 2(a) also shows that as the load increases, Z_{in_0} remains weakly capacitive, while Z_{in_1} remains weakly inductive. Moreover, the magnitude of the increase in the capacitive nature of Z_{in_0} is approximately four times that of the increase in the inductive nature of Z_{in_1}. Consequently, the hybrid matching architecture integrating dynamic LCC on the primary stationary side and static CS on the secondary rotational side ensures impedance robustness at the inverter output while maintaining a consistent, weakly inductive state under fluctuating load conditions. Under dynamic impedance matching, Fig. 2(b) shows that the magnitude of the LCC network equivalent input impedance (Z_{in}) increases approximately linearly with cutting force, while its phase initially decreases and then increases, yet remains overall weakly inductive. These impedance and phase characteristics under thermo-mechanical loads provide the basis for the subsequent control strategy.

https://doi.org/10.5194/ms-2026-209
Preprint. Discussion started: 27 November 2026
© Author(s) 2026. CC BY 4.0 License.



mechanical sciences DISCUSSIONS

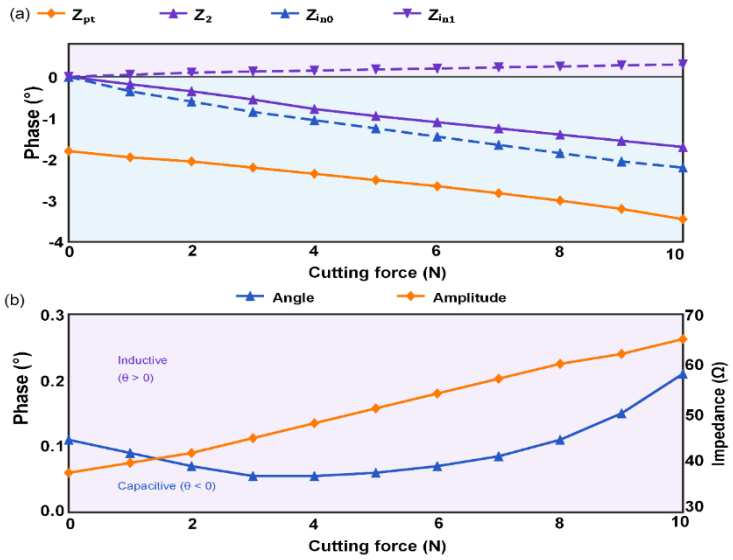

Figure 2: (a) The phase responses of Z_{PT}, Z_2, Z_{in_0}, and Z_{in_1} under variable cutting force loads; (b) The impedance magnitude and phase responses of Z_{in} under dynamic matching.

2.2 Load excitation characteristics

High-frequency piezoelectric ultrasonic transducers exhibit coupled thermo-mechanical load characteristics. As shown in Fig. 3, when the piezoelectric ceramic stack is maintained at 30 °C and 90 °C, and the cutting force varies from 0 to 10 N, the series resonance frequency f_s, static capacitance C_0, and motional resistance R_1 show approximately linear increases with cutting force. As shown in Fig. 3(a), the f_s at 90 °C is approximately 1.2 kHz lower than that at 30 °C under the same load, while the f_s values at both temperatures remain within 89.8–91.6 kHz. The same panel shows that C0 at 90 °C is approximately 0.2 nF higher than that at 30 °C under the same load and exhibits strong linearity within the 0–5 N range. Figure 3(b) shows that R_1 increases approximately linearly with cutting force at a rate of about 3 Ω/N over the 0–10 N range. Figure 3 further indicates that the BVD equivalent-circuit parameters exhibit strong linear relationships within the 0–8 N load range under different temperatures. Accordingly, the control boundary of the high-frequency rotary ultrasonic micromachining system is established within a linear range of 0–6 N. A cooling system is employed to maintain the operating temperature of the piezoelectric transducer, thereby mitigating thermal effects on resonant-frequency drift, static impedance matching, and load-induced perturbations.

https://doi.org/10.5194/ms-2026-209
Preprint. Discussion started: 27 November 2026
© Author(s) 2026. CC BY 4.0 License.

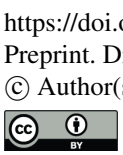

mechanical sciences
DISCUSSIONS

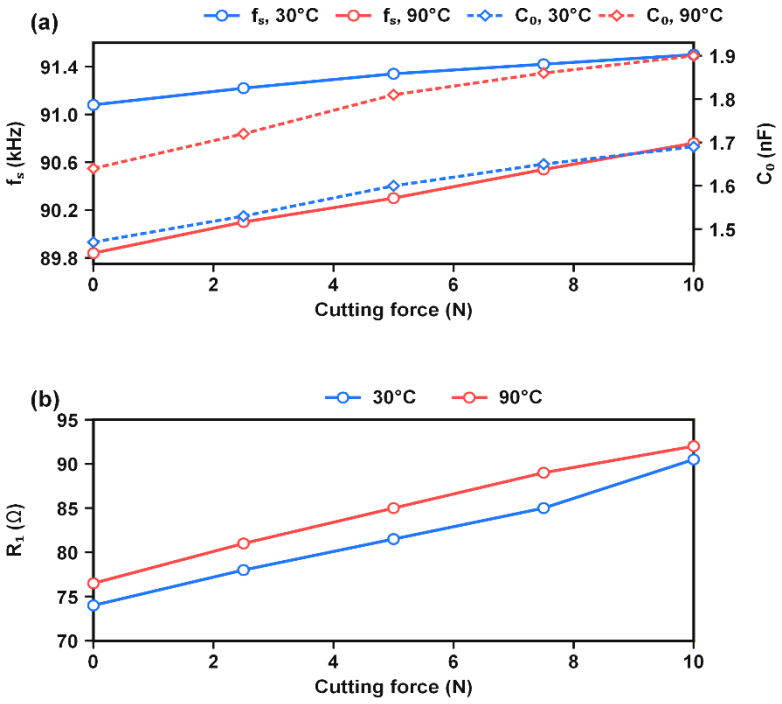

Figure 3: (a) Trends in the series resonant frequency f_s and static capacitance C_0 of the transducer under different temperatures and cutting-force loads; (b) trend in the motional resistance R_1 under different temperatures and cutting-force loads.

When the temperature of the piezoelectric ceramic stack is 60 °C, and the axial load falls within the range of 0–10 N, the mathematical relationship describing the response of the high-frequency longitudinal torsional piezoelectric ultrasonic transducer to the applied force is

$$\begin{cases} f_{s(\mathrm{Hz})} = 33.37F + 89487 \\ C_{0(\mathrm{nF})} = 0.003F + 1.463 \\ R_{1(\Omega)} = 3.080F + 37.22 \end{cases} \tag{6}$$

This equation establishes the mathematical relationship between the load force and the key parameters of the BVD equivalent circuit model, which is important for resonant frequency tracking. In addition to characterizing the frequency response of the piezoelectric ultrasonic transducer under varying loads, establishing the amplitude response under different loading conditions is essential for robust constant-amplitude regulation. The vibration amplitude of the piezoelectric ultrasonic transducer is generally proportional to the excitation current, which is regulated by a voltage-controlled current source.

When the axial load force is within the range of 0–10 N, the mathematical relationship between the force load corresponding to a constant-amplitude output and the drive voltage is as follows:

$$\begin{cases} U_{\mathrm{PT=0.5}} = 1.03F + 6.64 \\ U_{\mathrm{PT=1.0}} = 2.07F + 18.78 \\ U_{\mathrm{PT=1.5}} = 3.41F + 34.92 \end{cases} \tag{7}$$

https://doi.org/10.5194/ms-2026-209
Preprint. Discussion started: 27 November 2026
© Author(s) 2026. CC BY 4.0 License.



mechanical sciences
DISCUSSIONS

3 System control

Figure 4 illustrates the overall schematic of resonant frequency tracking based on the phase principle and amplitude tracking based on the constant-current principle. All electrical feedback signals are acquired from the stationary side of the ultrasonic spindle, including excitation frequency, excitation voltage and current amplitudes and root-mean-square (RMS) values, current RMS deviation, and voltage-current phase difference. The ensemble RBF-ELM neural network uses the loaded electromechanical equivalent circuit parameter model to predict external cutting forces and determine the reference setpoints for current adjustment (I_{ref}) and phase-locked regulation (θ_{ref}). The fuzzy PID controller then uses these setpoints to provide indirect load-side feedback when direct sensor-based measurement is unavailable, based on the pre-established electromechanical equivalent circuit database and RBF-ELM feature recognition. Meanwhile, electrical feedback enables resonant frequency tracking and constant-current regulation to maintain the transducer near its optimal resonant frequency, thereby improving energy transmission efficiency and electro-acoustic conversion quality.

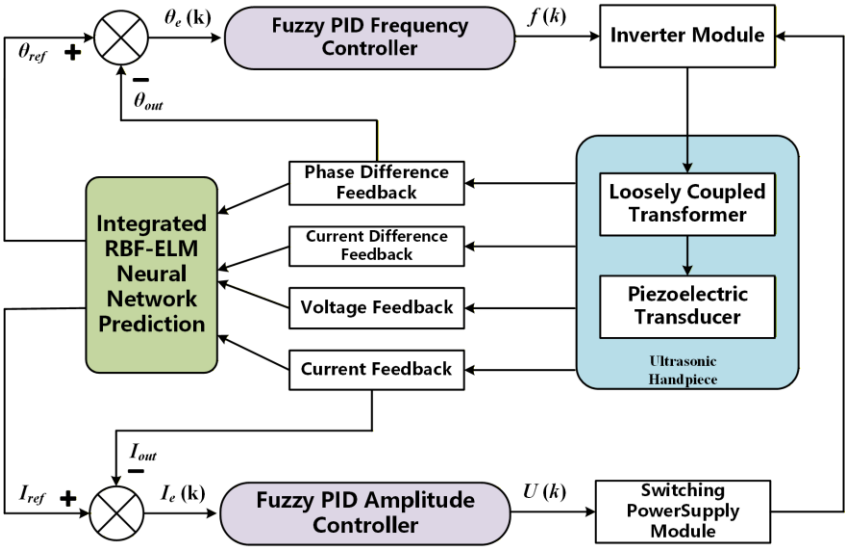

Figure 4: Block diagram of the control algorithm design.

Fuzzy PID control performs inference based on the error e and its rate of change ec to dynamically tune K_p, K_i, and K_d, thereby improving transient and steady-state performance. Gaussian, trapezoidal, and triangular membership functions are commonly used. Gaussian functions offer broad applicability and high stability but require greater computational effort, whereas trapezoidal and triangular functions provide faster execution (Du et al., 2021). To balance control stability and computational efficiency, a hybrid membership strategy is adopted: Gaussian membership functions are used for large e and ec to improve robustness, while triangular functions are applied for small e and ec to accelerate convergence and response near the steady state.

https://doi.org/10.5194/ms-2026-209
Preprint. Discussion started: 27 November 2026
© Author(s) 2026. CC BY 4.0 License.



mechanical sciences DISCUSSIONS

3.1 Fuzzy PID algorithms for resonant-frequency tracking and constant-amplitude control

In this section, the resonant frequency corresponding to the zero-phase point of the piezoelectric ultrasonic transducer is designated as the frequency tracking target. The fuzzy logic controller utilizes the phase difference (θ_e) and its rate of change (θ_{ec}) as input variables, while the control outputs are defined as the gain increments ΔK_{fp}, $\Delta K_{fi,}$ and ΔK_{fd}. The basic universes of discourse for these variables are defined as$\{B\theta_e\}$, $\{B\theta_e\}$, $\{\Delta BK_{fp}\}$, $\{\Delta BK_{fi}\}$, and$\{\Delta BK_{fd}\}$, respectively. Correspondingly, the fuzzy universes of discourse are denoted as $\{F\theta_e\}$, $\{F\theta_{ec}\}$, $\{\Delta FK_{fp}\}$, $\{\Delta FK_{fi}\}$, and $\{\Delta FK_{fd}\}$. The analytical relationship between the basic and fuzzy universes is expressed as follows:

$$\begin{cases} F\theta_e(k) = k_{fe} \cdot \theta_e(k) \\ F\theta_{ec}(k) = k_{fec} \cdot \theta_{ec}(k) \\ \Delta K_{fp}(k) = k_{fp} \cdot \Delta FK_{fp}(k) \\ \Delta K_{fi}(k) = k_{fi} \cdot \Delta FK_{fi}(k) \\ \Delta K_{fd}(k) = k_{fd} \cdot \Delta FK_{fd}(k) \end{cases} \tag{8}$$

In the equation, k_{fe}, k_{fec}, k_{fp}, k_{fi}, and k_{fd} are respectively the proportional factors of θ_e, θ_{ec}, ΔK_{fp}, ΔK_{fi}, and ΔK_{fd}. θ_e, θ_{ec}, ΔK_{fp}, ΔK_{fi}, and ΔK_{fd} correspond to the basic domains, fuzzy domains, and scaling factors shown in Table 1.

Table 1: Domains and scale factors for fuzzy PID frequency-tracking control.

Variable	θ_e	θ_{ec}	ΔK_{fp}	ΔK_{fi}	ΔK_{fd}
Basic domain	[-90, 90]	[-3E4, 3E4]	[-6E-3, 6E-3]	[-6E6, 6E6]	[-6E-5, 6E-5]
Fuzzy domain	[-3, 3]	[-3, 3]	[-3, 3]	[-3, 3]	[-3, 3]
Scale factor	0.0333	1E-4	0.002	2E6	2E-5

The fuzzy sets of the input variables θ_e and θ_{ec} adopt seven levels {NB, NM, NS, ZO, PS, PM, PB}, while the output variables ΔK_{fp}, ΔK_{fi}, and ΔK_{fd} use five levels {NB, NS, ZO, PS, PB}. The input and output membership functions for resonant frequency tracking are shown in Fig. 5, with Fig. 5(a) presenting the phase difference θ_e and its rate of change θ_{ec}, and Fig. 5(b) presenting the PID gain increments ΔK_{fp}, ΔK_{fi}, and ΔK_{fd}. The fuzzy inference controller processes θ_e and θ_{ec} to generate ΔK_{fp}, ΔK_{fi}, and ΔK_{fd} for dynamic tuning of the proportional, integral, and derivative gains of the PID controller. Under load fluctuations, the system selects appropriate PID gain increments. The fuzzy rules for resonant frequency tracking control are shown in Fig. 6.

https://doi.org/10.5194/ms-2026-209
Preprint. Discussion started: 27 November 2026
© Author(s) 2026. CC BY 4.0 License.

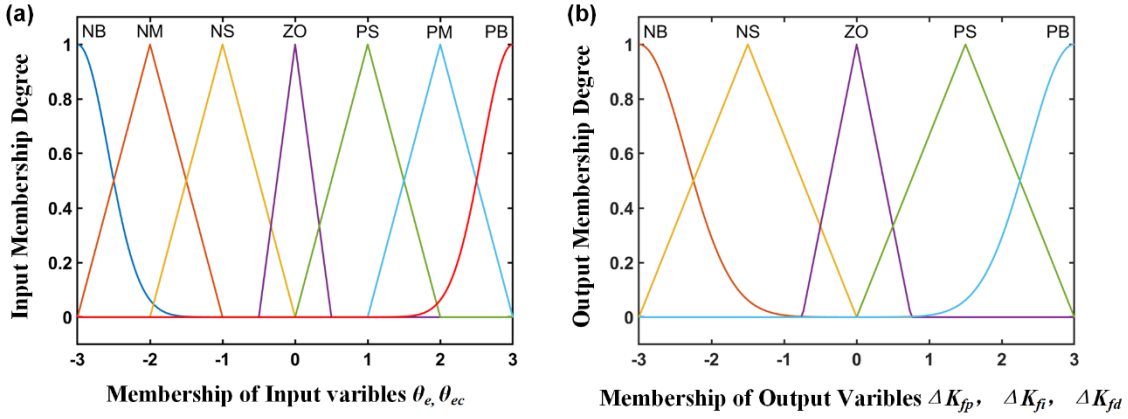

Figure 5: Input and output membership functions of the fuzzy logic controller in frequency tracking.

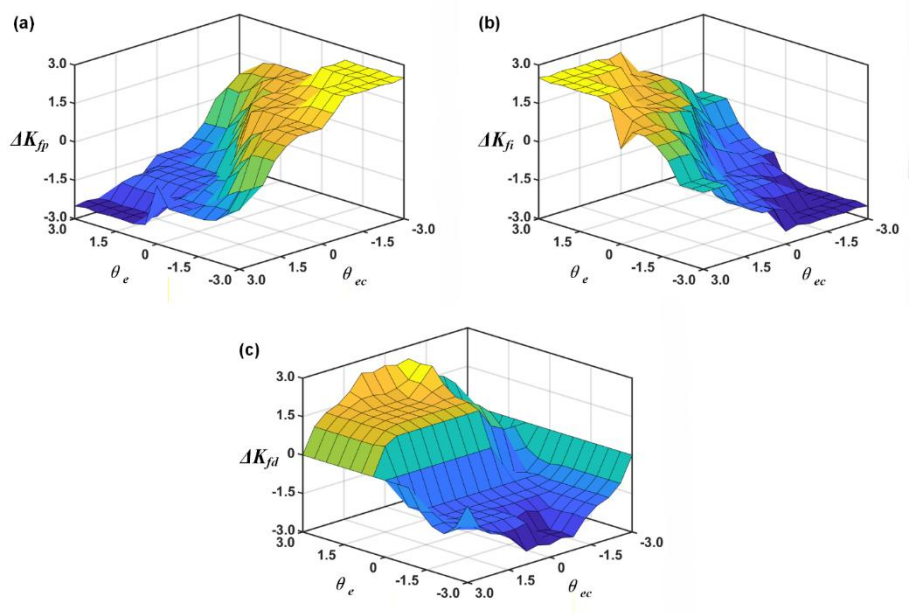

Figure 6: Fuzzy rules of resonant-frequency tracking control.

As illustrated in Fig. 7, when the phase difference θ_e and its rate of change θ_{ec} undergo large variations, the gain increments ΔK_{fp}, ΔK_{fi}, and ΔK_{fd} are adaptively increased to accelerate phase convergence toward the target and reduce transient deviations during load transitions. Fixed tuning increments may cause oscillations around the new equilibrium. As θ_e decreases, the fuzzy inference engine correspondingly reduces the PID gain increments to suppress overshoot and maintain the phase error within the allowable steady-state range, thereby improving resonant frequency tracking accuracy. The control law for the fuzzy PID resonant frequency tracking algorithm is expressed as:

$$\begin{cases} f(k) = f(k-1) + \Delta f(k) \\ \Delta f(k) = K_{fp}[\theta_e(k) - \theta_e(k-1)] + K_{fi}\theta_e(k) + K_{fd}[\theta_e(k) - 2\theta_e(k-1) + \theta_e(k-2)] \end{cases} \quad (9)$$

https://doi.org/10.5194/ms-2026-209
Preprint. Discussion started: 27 November 2026
© Author(s) 2026. CC BY 4.0 License.

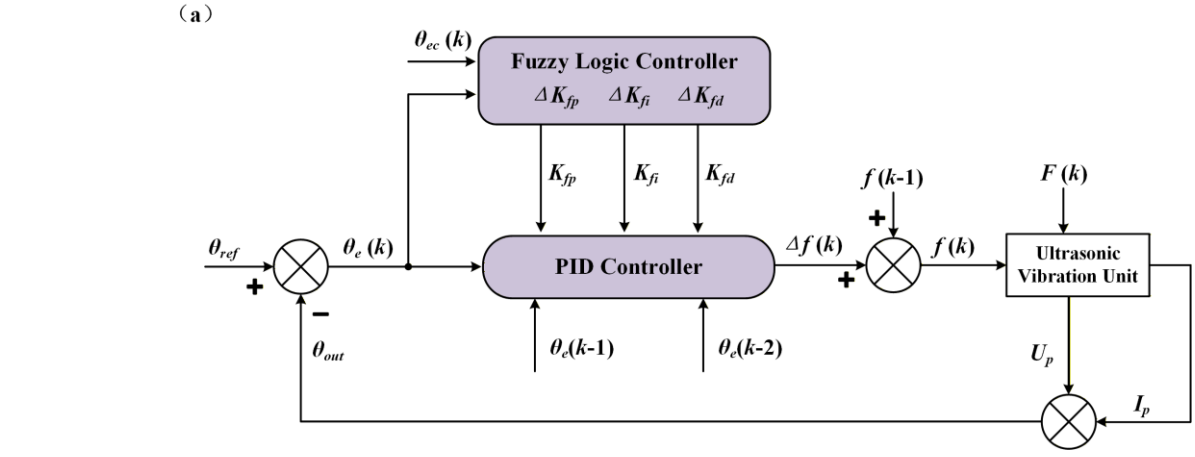

Figure 7: Principle of the fuzzy PID frequency-tracking control algorithm.

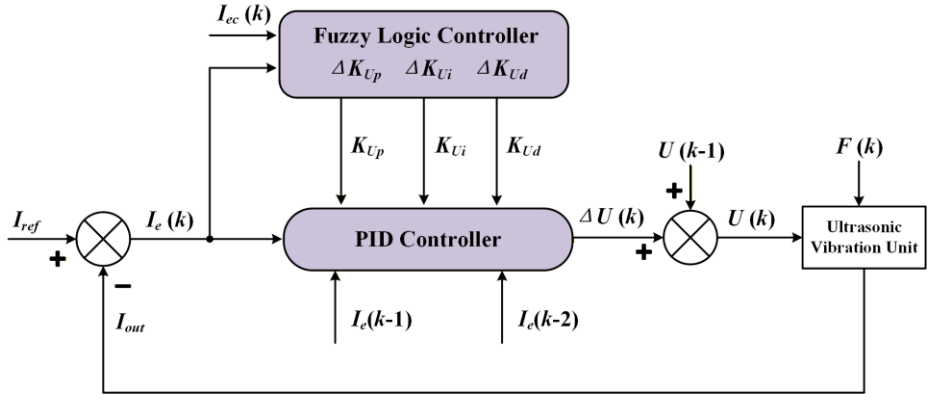

Figure 8: Principle of the fuzzy PID constant-amplitude control algorithm.

During high-precision microstructure machining, stable ultrasonic vibration amplitude under varying loads is essential. Since the vibration amplitude is proportional to the excitation current, the current corresponding to the desired amplitude is set as the reference for constant-amplitude control. A voltage-controlled current source regulates the current to remain approximately constant during machining. As shown in Fig. 8, the fuzzy logic controller dynamically adjusts the PID parameters K_{Up}, K_{Ui}, and K_{Ud}. When the RMS current error I_e and its rate of change I_{ec} vary significantly, the gain increments are increased to accelerate convergence toward the reference current and reduce transient response time. As the current approaches the reference, the gain increments are reduced to suppress overshoot and maintain I_e within the allowable steady-state range, thereby improving amplitude regulation stability. The excitation current is regulated by the control voltage of the ultrasonic driver; consequently, the control law for the fuzzy PID constant-amplitude regulation algorithm is expressed as follows:

$$\begin{cases} U(k) = U(k-1) + \Delta U(k) \\ \Delta U(k) = K_{Up}[I_e(k) - I_e(k-1)] + K_{Ui}I_e(k) + K_{Ud}[I_e(k) - 2I_e(k-1) + I_e(k-2)] \end{cases} \quad (10)$$

https://doi.org/10.5194/ms-2026-209
Preprint. Discussion started: 27 November 2026
© Author(s) 2026. CC BY 4.0 License.



mechanical sciences DISCUSSIONS

In the equation, the parameters K_{Up}, $K_{Ui,}$ and K_{Ud} are respectively.

$$\begin{cases} K_{Up} = \Delta K_{Up} + K_{Up0} \\ K_{Ui} = \Delta K_{Ui} + K_{Ui0} \\ K_{Ud} = \Delta K_{Ud} + K_{Ud0} \end{cases} \tag{11}$$

In the equation, the parameters ΔK_{Up}, ΔK_{Ui}, and ΔK_{d} represent the changes in the proportional gain, integral gain, and derivative gain of the fuzzy inference controller, respectively. The parameters K_{Up0}, K_{Ui0}, and K_{Ud0} are the initial gain values of the fuzzy PID controller.

The inputs of the fuzzy logic controller are I_e and I_{ec}, and its outputs are ΔK_p, ΔK_i, and ΔK_d. The parameters I_e, I_{ec}, ΔK_{Up}, ΔK_{Ui}, and ΔK_{Ud} correspond to the basic fuzzy control domain $\{BI_e\}$, $\{BI_{ec}\}$, $\{\Delta IK_{Up}\}$, $\{\Delta IK_{Ui}\}$, $\{\Delta IK_{Ud}\}$, with corresponding fuzzy domains being $\{FI_e\}$,$\{FI_{ec}\}$,$\{\Delta FK_{Up}\}$,$\{\Delta FK_{Ui}\}$, and $\{\Delta FK_{Ud}\}$. The analytical relationship between the basic universes and their fuzzy counterparts is expressed as follows:

$$\begin{cases} FI_e(k) = k_{Ie} \cdot I_e(k) \\ FI_{ec}(k) = k_{Iec} \cdot I_{ec}(k) \\ \Delta K_{Up}(k) = k_{Ip} \cdot \Delta FK_{Up}(k) \\ \Delta K_{Ui}(k) = k_{Ii} \cdot \Delta FK_{Ui}(k) \\ \Delta K_{d}(Uk) = k_{Id} \cdot \Delta FK_{Ud}(k) \end{cases} \tag{12}$$

In the equation, k_{Ie}, k_{Iec}, k_{Ip}, k_{Ii}, and k_{Id} represent the parameters I_e, I_{ec}, ΔK_{Up}, ΔK_{Ui}, and ΔK_{Ud}, respectively. And I_e, I_{ec}, ΔK_{Up}, ΔK_{Ui}, and ΔK_{Ud} correspond to the basic domain, fuzzy domain, and scaling factor, as shown in Table 2.

Table 2: Domains and scale factors for fuzzy PID constant-amplitude control.

Variable	I_e	I_{ec}	ΔK_{Up}	ΔK_{Ui}	ΔK_{Ud}
Basic domain	[-2, 2]	[-1E3, 1E3]	[-0.05, 0.05]	[-3E6, 3E6]	[-4E-5, 4E-5]
Fuzzy domain	[-1, 1]	[-1, 1]	[-1, 1]	[-1, 1]	[-1, 1]
Scale factor	0.5	1E-3	0.05	3E6	4E-5

Load fluctuations in rotary ultrasonic micromachining cause significant impedance variations in the piezoelectric transducer. Under a constant driver output voltage, these variations lead to instability in the excitation current and vibration amplitude, degrading machining quality. Because high-frequency rotary ultrasonic spindles operate at high speeds, even transient amplitude fluctuations can affect surface integrity and cause machining defects. Therefore, constant-current regulation requires high dynamic responsiveness to maintain stable processing. To reduce the computational burden of multiple fuzzy levels, a simplified three-level fuzzy partition {NS, ZO, PS} is adopted for the FLC inputs I_e and I_{ec} and the output gain increments ΔK_{Up}, ΔK_{Ui}, and ΔK_{Ud}. Triangular membership functions are used for their low computational complexity, enabling rapid execution and high-speed regulation in high-frequency RUM.

https://doi.org/10.5194/ms-2026-209
Preprint. Discussion started: 27 November 2026
© Author(s) 2026. CC BY 4.0 License.

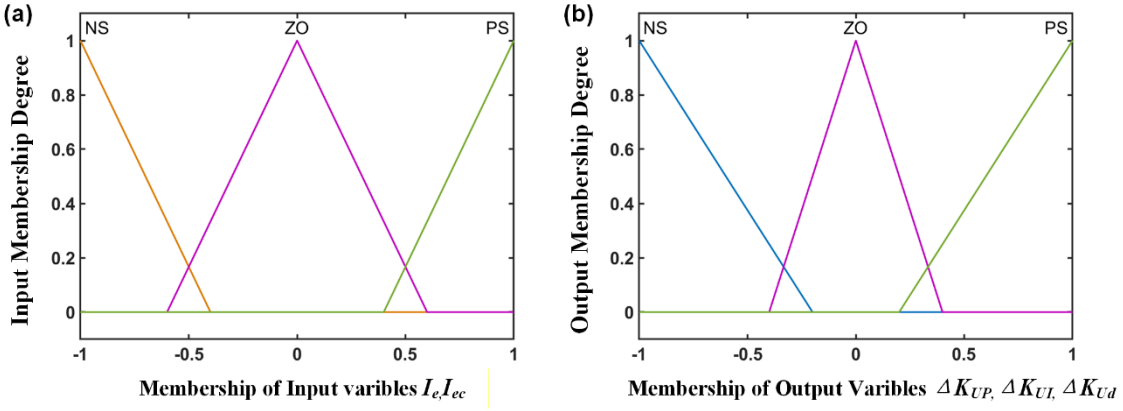

Figure 9: Input and output membership functions of the fuzzy logic controller in constant-amplitude control.

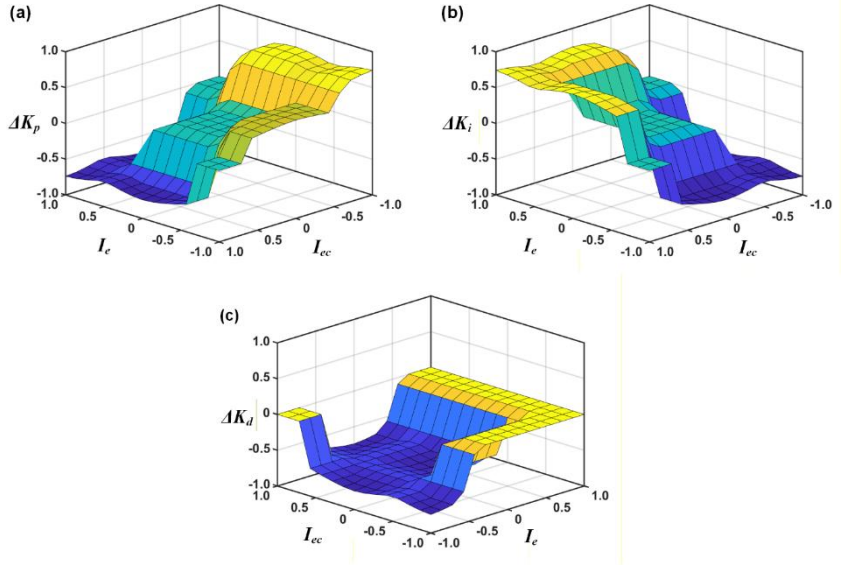

Figure 10: Fuzzy rules of constant-amplitude control.

3.2 Neural-network-based load characteristic prediction model

In rotary ultrasonic machining and related vibration-assisted processes, direct cutting-force measurement and real-time feedback remain challenging. Neural-network-based online prediction can overcome hardware sensing limitations and support closed-loop control of ultrasonic machining systems. Online prediction methods include Artificial Neural Networks, Support Vector Machines, and Extreme Learning Machines (Wang et al., 2022). The Extreme Learning Machine (ELM) uses a single-hidden-layer feedforward network and requires only the number of hidden-layer neurons to be specified, reducing manual parameter tuning. Its fast convergence, training speed, and closed-form solution for output weights make ELM suitable for high-frequency real-time control (Liu and Wan, 2015).

https://doi.org/10.5194/ms-2026-209
Preprint. Discussion started: 27 November 2026
© Author(s) 2026. CC BY 4.0 License.



mechanical sciences DISCUSSIONS

The ensemble ELM neural network consists of multiple ELM models combined through weighted strategies to improve the mapping between input features and output labels. Radial basis function (RBF) neural networks provide nonlinear approximation, good generalization, and fast convergence. As shown in Fig. 11, K_1, K_2, ..., K_m denote the radial basis functions. The RBF-ELM network incorporates RBFs into the ELM framework, allowing the RBF centers and widths to be rapidly determined by the ELM method and enabling efficient processing of large-scale data. This combination improves the network's ability to approximate nonlinear mappings while enhancing its accuracy, robustness, and predictive performance in high-frequency RUM (Li et al., 2021).

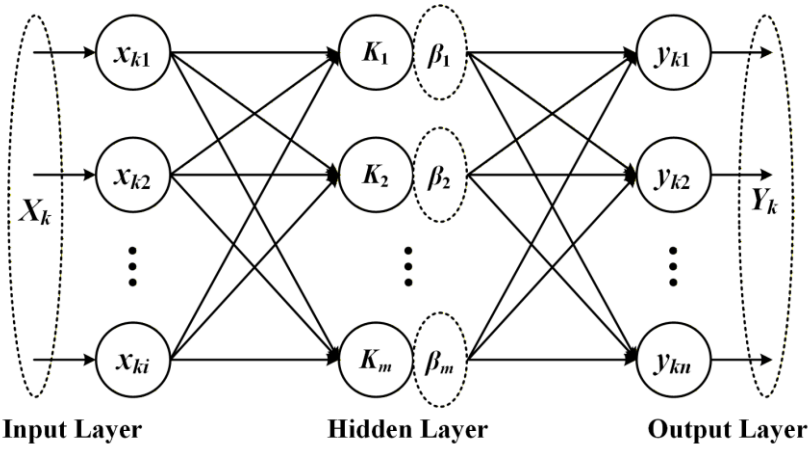

Figure 11: RBF-ELM neural network architecture.

This section uses an integrated ELM neural network to predict and evaluate load forces, training multiple sub-networks with different radial basis functions and expansion widths. RBF-ELM derives the transient stability assessment results by comprehensively evaluating the output load forces of multiple sub-RBF-ELMs. The ultrasonic vibration system acquires feedback signals in the form of current amplitude and the phase difference between current and voltage; the two radial basis functions corresponding to these signals are:

Gaussian function:

$$K(x,\mu_i) = exp(\frac{-||x-\mu_i||^2}{\sigma^2}) \tag{13}$$

Inverse of a quadratic function:

$$K(x,\mu_i) = \frac{1}{\sqrt{1+||x-\mu_i||^2/\sigma^2}} \tag{14}$$

In the equation, x represents the input feature, μ_i denotes the center of the i kernel function, the samples are uniformly drawn from the bounding hyperrectangle of the input feature, and σ represents the expansion width parameter.

The expected output matrix T_{ep} of the training dataset can be represented as an n×1 column vector.

$$T_{ep} = (t_1, t_2, \cdots, t_n)^T \tag{15}$$

https://doi.org/10.5194/ms-2026-209
Preprint. Discussion started: 27 November 2026
© Author(s) 2026. CC BY 4.0 License.



mechanical sciences DISCUSSIONS

The expected output matrix T_{ep} can be calculated using the formula.

$$H_{hl}\beta_w = T_{ep} \tag{16}$$

In the expressions above, H_{hl} denotes the n×m hidden layer output matrix, while β_w represents the m×1 weight vector connecting the hidden and output layers. These parameters are determined according to the following analytical formulations:

$$H_{hl} = \begin{bmatrix} K(x_1,\mu_1) & K(x_1,\mu_2) & \cdots & K(x_1,\mu_m) \\ K(x_2,\mu_1) & K(x_2,\mu_2) & \cdots & K(x_2,\mu_m) \\ \vdots & \vdots & \ddots & \vdots \\ K(x_n,\mu_1) & K(x_n,\mu_2) & \cdots & K(x_n,\mu_m) \end{bmatrix} \tag{17}$$

$$\beta_w = (\beta_1, \beta_2, \cdots, \beta_m)^T \tag{18}$$

When H_{hl} is a reversible matrix, the number of training samples equals the number of neurons in the hidden layer, i.e., n = m, and we have

$$\beta_w = H_{hl}^{-1} T_{ep} \tag{19}$$

Equation (19) shows that the network perfectly fits the mapping relationship between the input and output with zero error. However, the number of training samples is usually much larger than the number of hidden layer neurons, that is, n > m; then H_{hl} is irreversible, so there is no β_w such that Eq. (19) holds. At this time, the least squares method can be used to solve the following formula to obtain the optimal solution of β_w:

$$\min_{\beta_w} \left\| H_{hl}\beta_w - T_{ep} \right\| \tag{20}$$

The least-squares solution of Eq. (20) is represented as

$$\hat{\beta}_w = H^{\dagger} T_{ep} \tag{21}$$

In the equation, the pseudoinverse of the matrix H_{hl} (i.e., the (M-P)-augmented inverse of the matrix H_{hl}) can be calculated using the orthogonal method.

$$H^{\dagger} = \begin{cases} (H_{hl}^T H_{hl})^{-1} H_{hl}^T, & H_{hl}^T H_{hl} \text{ invertible} \\ H_{hl}^T (H_{hl} H_{hl}^T)^{-1}, & H_{hl} H_{hl}^T \text{ invertible} \end{cases} \tag{22}$$

Find the least-squares solution in canonical form. Afterward, the parameters of the RBF-ELM neural network can be trained. For any input sample, the corresponding model output values are represented as

$$Y^{\forall} = H_{hl}(X^{\forall})\hat{\beta}_w \tag{23}$$

3.3 Integration mechanisms and predictive assessment

To improve cutting force estimation accuracy and prediction robustness, the ensemble RBF-ELM framework incorporates two sub-models with different radial basis functions and expansion widths (σ). Compared with a single RBF-ELM, the ensemble model reduces information loss by combining the distinct mapping rules learned by the sub-models and integrating

https://doi.org/10.5194/ms-2026-209
Preprint. Discussion started: 27 November 2026
© Author(s) 2026. CC BY 4.0 License.

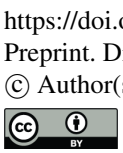

mechanical sciences DISCUSSIONS

their outputs to estimate the transient cutting force. The working mechanism of the multi-RBF-ELM integrated network is shown in Fig. 12.

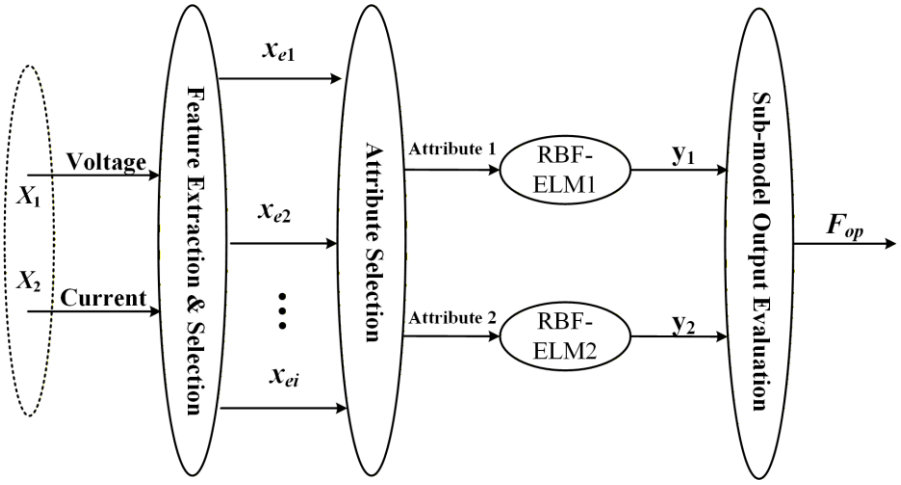

Figure 12: Working mechanism of the integrated RBF-ELM model.

Figure 12 includes two raw electrical parameter samples, X_1 and X_2, which are utilized to establish reference setpoints for constant-amplitude and frequency tracking control. x_{e1}, x_{e2}, …, x_{ei} denote the i key features obtained through feature selection, primarily encompassing the root-mean-square (RMS) voltage, RMS current, the current difference I_e between two consecutive samples, and the phase difference θ_e between voltage and current. Attribute 1 and Attribute 2 denote the radial basis functions and σ parameters selected for RBF-ELM1 and RBF-ELM2, respectively. y_1 and y_2 represent the transient cutting force prediction results of RBF-ELM1 and RBF-ELM2 for the samples, respectively; these outputs are then evaluated to yield the optimal predicted cutting force F_{op}. The system maps F_{op} to the established load-response relationships of the ultrasonic spindle, subsequently generating I_{ref} and θ_{ref} as the input reference setpoints for fuzzy PID control. The training of the ensemble RBF-ELM framework utilizes the resonant frequencies and excitation current values of the piezoelectric ultrasonic transducer acquired under varying cutting forces. Following data acquisition, a normalization process is implemented to ensure feature consistency and accelerate model convergence. Subsequently, eight groups of the corresponding parameters, obtained under distinct load conditions, are designated as the testing dataset to evaluate and validate the model's predictive performance. As illustrated in Fig. 13, the simulation results demonstrate that the methodology possesses high estimation accuracy and learning velocity, enabling the prediction of the specific magnitude of the cutting force. However, when cutting force fluctuations exceed 5 N, the estimated value is approximately 0.7 N higher than the actual force. The primary reason is that the prediction process neglects the inductive, capacitive, and stray losses within the ultrasonic spindle and circuit systems, which leads to a larger predicted current value and a correspondingly larger predicted load force.

https://doi.org/10.5194/ms-2026-209
Preprint. Discussion started: 27 November 2026
© Author(s) 2026. CC BY 4.0 License.



mechanical sciences DISCUSSIONS

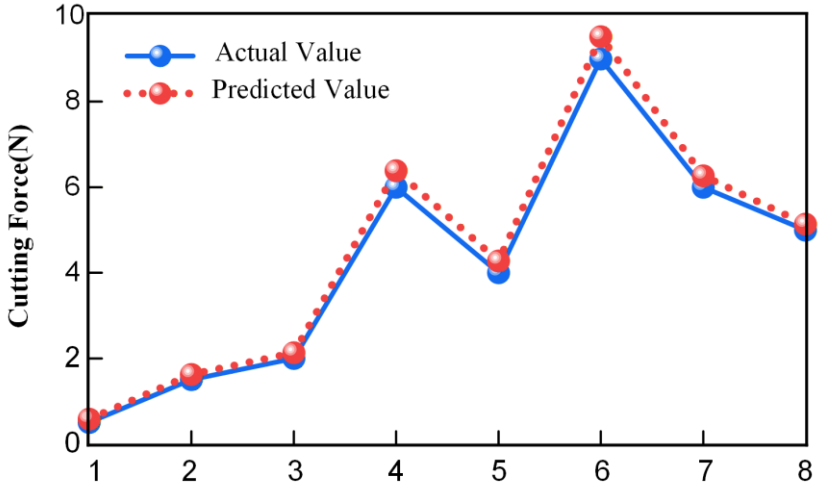

Figure 13: Prediction results from the integrated RBF-ELM neural network.

4 Conclusions

This study investigates the load-dependent characteristics of a high-frequency rotary ultrasonic micromachining system and establishes a load prediction-based adaptive control strategy using an LCC-CS bilateral impedance matching network. The main conclusions are summarized as follows:

(1) The load-dependent characteristics of the high-frequency longitudinal-torsional composite piezoelectric ultrasonic transducer are investigated under thermo-mechanical coupling conditions. The relationships between axial loads (0–10 N) and key electromechanical parameters (f_s, C_0, and R_m) are obtained to support frequency tracking, impedance compensation, and amplitude regulation.

(2) The impedance characteristics of the LCC-CS bilateral impedance matching ultrasonic vibration system are analyzed under different cutting forces, revealing the relationships among load, impedance magnitude, phase response, and resonant frequency.

(3) An ensemble RBF-ELM model predicts cutting forces in real time and updates resonant frequency and excitation current references. Fuzzy PID control rules adapt to different load conditions to achieve stable frequency tracking and constant-amplitude regulation.

Code and data availability

The original data and simulation model files underlying the reported results could not be located and are therefore currently unavailable.

https://doi.org/10.5194/ms-2026-209
Preprint. Discussion started: 27 November 2026
© Author(s) 2026. CC BY 4.0 License.



mechanical sciences
DISCUSSIONS

Author contributions

KZ conceptualized the study, developed the methodology, supervised the research, and acquired funding. GZ developed the model and software, performed formal analysis, and prepared the original draft. YX performed validation and reviewed and edited the manuscript. GC provided resources, performed validation, and reviewed and edited the manuscript. JG curated the data and performed formal analysis. XA contributed to the methodology and supervision and reviewed and edited the manuscript.

Competing interests

The authors declare that they have no conflict of interest.

Financial support

This research has been supported by the Key Technologies Research and Development Program of Henan Province (grant no. 262102221031).

References

Ansary, S.R., Kabir, S., Nnokwe, C., He, R., Pei, Z., and Cong, W.: Fabrication of micro-grooves in silicon wafers using rotary ultrasonic micromachining: Parametric effects of different vibration modes, J Manuf Process, 155, 12–25, https://doi.org/10.1016/j.jmapro.2025.09.045, 2025.

Du, P., Liu, Y., Chen, W., Zhang, S., and Deng, J.: Fast and Precise Control for the Vibration Amplitude of an Ultrasonic Transducer Based on Fuzzy PID Control, IEEE Trans Ultrason Ferroelectr Freq Control, 68, 2766–2774, https://doi.org/10.1109/TUFFC.2021.3078663, 2021.

Du, P., Chen, W., Deng, J., Zhang, S., Zhang, J., and Liu, Y.: A critical review of piezoelectric ultrasonic transducers for ultrasonic-assisted precision machining, Ultrasonics, 135, 107145, https://doi.org/10.1016/j.ultras.2023.107145, 2023.

Duan, Z., Chen, T., Suo, Y., Pan, X., and Pan, X.: Research on the performance of frequency tracking methods for the ultrasonic machining system considering the influence of the impedance matching unit, Appl Acoust, 231, 110439, https://doi.org/10.1016/j.apacoust.2024.110439, 2025.

Jiang, X., Ye, H., Yu, B., and Hu, X.: Research on optimization of LCC-S compensation network parameters for rotary ultrasonic machining under varying loads, Measurement, 256, 118425, https://doi.org/10.1016/j.measurement.2025.118425, 2025.

Li, Q., Xiong, Q., Ji, S., Yu, Y., Wu, C., and Yi, H.: A method for mixed data classification based on the RBF-ELM network, Neurocomputing, 431, 7–22, https://doi.org/10.1016/j.neucom.2020.12.032, 2021.

https://doi.org/10.5194/ms-2026-209
Preprint. Discussion started: 27 November 2026
© Author(s) 2026. CC BY 4.0 License.



mechanical sciences
DISCUSSIONS

Lin, C.-H., Lu, Y., Chiu, H.-J., and Ou, C.-L.: Eliminating the temperature effect of the piezoelectric transformer in the backlight electronic ballast by applying the digital phase-locked-loop technique, IEEE Trans Ind Electron, 54, 1024–1031, https://doi.org/10.1109/TIE.2007.892733, 2007.

Lin, C.-J., Jhang, J.-Y., and Lin, X.-Q.: Designing an Ultrasonic-Assisted Machining System by Using a Network Mapping Fusion-Convolutional Neuro-Fuzzy Network Model, IEEE Trans Ind Inform, 20, 9286–9297, https://doi.org/10.1109/TII.2024.3383866, 2024.

Liu, X. and Wan, A.: Universal consistency of extreme learning machines for the RBFNs case, Neurocomputing, 168, 1132–1137, https://doi.org/10.1016/j.neucom.2015.05.010, 2015.

Liu, X., Colli-Menchi, A.I., Gilbert, J., Friedrichs, D.A., Malang, K., and Sanchez-Sinencio, E.: An Automatic Resonance Tracking Scheme With Maximum Power Transfer for Piezoelectric Transducers, IEEE Trans Ind Electron, 62, 7136–7145, https://doi.org/10.1109/TIE.2015.2436874, 2015.

Ma, S., Zhang, Y., Zhuang, X., Wang, D., Chen, S., and Liu, H.: Frequency tuning and automatic frequency tracking of shunted piezoelectric transducers, Ultrasonics, 141, 107318, https://doi.org/10.1016/j.ultras.2024.107318, 2024.

Mostaghimi, H., Park, S. S., Lee, D. Y., Nam, S., and Nam, E.: Prediction of Tool Tip Dynamics Through Machine Learning and Inverse Receptance Coupling, Int. J. Precis. Eng. Manuf., 24, 1739–1752, https://doi.org/10.1007/s12541-023-00831-6, 2023.

Peng, T., Jiang, Z., Li, X., Li, Y., and Long, Z.: Dual closed-loop amplitude control based on fuzzy and expert PI for high-power ultrasonic machining under variable load, Appl Acoust, 231, 110428, https://doi.org/10.1016/j.apacoust.2024.110428, 2025.

Quan, Q., Wang, T., Yu, H., Deng, Q., Tang, D., and Deng, Z.: An Ultrasonic Drilling System for Fast Drilling Speed With Uncertain Load, IEEE-ASME Trans Mechatron, 28, 1477–1487, https://doi.org/10.1109/TMECH.2022.3228593, 2023.

Tang, X., Chen, Z., Zheng, S., Chen, H., Zhao, X., and Kong, Y.: Design of Compensation Network and Parameter Optimization for Rotary Ultrasonic Machining Under Varying Loads, IEEE Trans Power Electron, 38, 14747–14760, https://doi.org/10.1109/TPEL.2023.3304362, 2023.

Wang, J., Jiang, J., Duan, F., Zhang, F., Liu, W., and Qu, X.: A Novel Fast Resonance Frequency Tracking Method Based on the Admittance Circle for Ultrasonic Transducers, IEEE Trans Ind Electron, 67, 6864–6873, https://doi.org/10.1109/TIE.2019.2938476, 2020.

Wang, J., Lu, S., Wang, S.-H., and Zhang, Y.-D.: A review of extreme learning machines, Multimed Tools Appl, 81, 41611–41660, https://doi.org/10.1007/s11042-021-11007-7, 2022.

Wang, L., Yan, M., Liu, Y., and Wang, D.: Amplitude-Phase control algorithm based on fuzzy PI against vibration fluctuation of ultrasonic surgical instruments, Appl Acoust, 231, 110489, https://doi.org/10.1016/j.apacoust.2024.110489, 2025.

Xu, S., Kuriyagawa, T., Shimada, K., and Mizutani, M.: Recent advances in ultrasonic-assisted machining for the fabrication of micro/nano-textured surfaces, Front Mech Eng, 12, 33–45, https://doi.org/10.1007/s11465-017-0422-5, 2017.

https://doi.org/10.5194/ms-2026-209
Preprint. Discussion started: 27 November 2026
© Author(s) 2026. CC BY 4.0 License.



mechanical sciences
DISCUSSIONS

390 Zhang, C., Rentsch, R., and Brinksmeier, E.: Advances in micro ultrasonic assisted lapping of microstructures in hard-brittle materials: a brief review and outlook, Int J Mach Tools Manuf, 45, 881–890, https://doi.org/10.1016/j.ijmachtools.2004.10.018, 2005.

Zhang, K., Gao, G., Zhao, C., Wang, Y., Wang, Y., and Li, J.: Review of the design of a power ultrasonic generator for a piezoelectric transducer, Ultrason Sonochem, 96, 106438, https://doi.org/10.1016/j.ultsonch.2023.106438, 2023.

395 Zhang, K., Gao, G., Ma, W., Li, R., Xiang, D., and Ma, J.: A thermo-mechanical coupling load model for a high-frequency piezoelectric ultrasonic transducer, Ultrason Sonochem, 111, 107148, https://doi.org/10.1016/j.ultsonch.2024.107148, 2024a.

Zhang, K., Gao, G., Wang, Y., Wang, Y., Wang, G., Xiang, Y., Wu, Z., and Xiang, D.: An LCC-CS bilateral matching network for high efficiency energy conversion in high-frequency piezoelectric rotary ultrasonic machining system, Measurement, 238, 115391, https://doi.org/10.1016/j.measurement.2024.115391, 2024b.

400 Zhu, Y., Yang, T., Fang, Z., and Yang, M.: An Ultra-Fast Transient Performance Tracking Scheme for High-Power Piezoelectric Transducers, IEEE Trans Power Electron, 41, 1879–1890, https://doi.org/10.1109/TPEL.2025.3604829, 2026.